



HAL
open science

Modelling of hydrogen isotopes trapping, diffusion and permeation in divertor monoblocks under ITER-like conditions

E.A. Hodille, Rémi Delaporte-Mathurin, J. Denis, M. Pecovnik, E. Bernard, Y. Ferro, R. Sakamoto, Y. Charles, J. Mougenot, A. de Backer, et al.

► To cite this version:

E.A. Hodille, Rémi Delaporte-Mathurin, J. Denis, M. Pecovnik, E. Bernard, et al.. Modelling of hydrogen isotopes trapping, diffusion and permeation in divertor monoblocks under ITER-like conditions. Nuclear Fusion, 2021, 61 (12), pp.126003. 10.1088/1741-4326/ac2abc . hal-03400941

HAL Id: hal-03400941

<https://hal.science/hal-03400941>

Submitted on 25 Oct 2021

HAL is a multi-disciplinary open access archive for the deposit and dissemination of scientific research documents, whether they are published or not. The documents may come from teaching and research institutions in France or abroad, or from public or private research centers.

L'archive ouverte pluridisciplinaire **HAL**, est destinée au dépôt et à la diffusion de documents scientifiques de niveau recherche, publiés ou non, émanant des établissements d'enseignement et de recherche français ou étrangers, des laboratoires publics ou privés.



Distributed under a Creative Commons Attribution - NonCommercial - NoDerivatives 4.0 International License

Modelling of hydrogen isotopes trapping, diffusion and permeation in divertor monoblocks under ITER-like conditions

E A Hodille¹, R. Delaporte-Mathurin^{1,2}, J. Denis³, M. Pecovnik⁴, E. Bernard¹, Y. Ferro³, R. Sakamoto⁵, Y. Charles², J. Mougenot², A. De Backer², C. S. Becquart⁶, S. Markelj⁴, C. Grisolia¹

¹ CEA, IRFM, F-13108 Saint Paul Lez Durance, France

² Université Sorbonne Paris Nord, Laboratoire des Sciences des Procédés et des Matériaux, LSPM, CNRS, UPR 3407, F-93439, Villetaneuse, France

³ Aix Marseille Univer., CNRS, PIIM, F-13013 Marseille, France

⁴ Jožef Stefan Institute, Jamova cesta 39, 1000 Ljubljana, Slovenia

⁵ NINS, National Institute for Fusion Science, Toki, Gifu 509-5292, Japan

⁶ Univ. Lille, CNRS, INRAE, Centrale Lille, UMR 8207 - UMET - Unité Matériaux et Transformations, F-59000 Lille, France

E-mail: etienne.hodille@gmail.com

Abstract. In this work, the deuterium (D) retention in plasma facing components of the divertor of ITER is estimated. Three scenarios are simulated with 3 different surface temperatures, 1456 K, 870 K and 435 K. They represent the exposure of different parts of the divertor during an attached plasma. Our 1D rate equation code MHIMS (migration of hydrogen in materials) is used to model the retention in the super-saturated layer formed in the first 10 nm: the D retention integrated in this 10-nm-layer is $\approx 10^{19}$ Dm⁻² for the coldest scenarios. It is also used to differentiate the evolution of deuterium retention during pulsed and continuous plasma exposures which shows that: (i) there is a retention during the ramp-down in the first 10 μ m which is released during the ramp up and (ii) the bulk retention is not affected by the cycling of plasma exposure. The concentration of mobile deuterium in the implantation zone is used as an input of our finite element code FESTIM (finite element simulation of tritium in materials) which is used to assess the deuterium retention and migration in the 2D complex geometry of the actively cooled plasma facing components. In the end, this work enables to determine the three following macroscopic quantities: the total deuterium retention, the permeation flux to the cooling pipe and the desorption flux from the toroidal edges of the components. It is shown that (i) the coldest scenario leads to the highest retention despite the lowest exposure flux which has already been observed in past retention studies, (ii) the permeation to the cooling pipes happens after few thousands of seconds only for the hottest scenario, (iii) the release of deuterium from the toroidal edges is a small fuel recycling source.

Keywords : Hydrogen, materials, plasma material interactions, modelling

1. Introduction

In a tokamak, the plasma facing components are exposed to intense fluxes of particles ($\approx 10^{24} \text{ m}^{-2}\text{s}^{-1}$) and heat ($\approx 10 \text{ MWm}^{-2}$) [1]. The divertor will experience the most intense plasma wall interaction. To sustain such harsh environment in steady state condition (minutes long plasma discharges), a tungsten (W) armor has been chosen which is actively cooled by a water navigating at 343 K in a copper alloys (CuCrZr) tube. In order to reduce mechanical incompatibilities between both materials [2], a Cu inter layer is used. This is the design of the divertor plasma facing components of WEST [3] and ITER.

This intense particle flux leads to the implantation and further trapping of hydrogen isotopes in the divertor monoblocks increasing the content of hydrogen in the wall elements of the tokamak. This causes two main issues: i) A fusion plasma contains ideally an equal mixture of tritium and deuterium. The tritium being a radioactive element, the safety authority limits its overall inventory in the vacuum chamber of ITER to 700 g. ii) The fuel retained in the wall can act as an unpredictable source of plasma particles that can affect the core plasma: an uncontrolled outgassing from the wall element, especially during long pulses discharges (>minutes) can cause uncontrolled increase of the plasma density leading ultimately to its termination [4]. It is thus crucial to understand the mechanisms leading to fuel retention, release and permeation in plasma facing materials.

This work tackles this issue using macroscopic diffusion/reaction models based on the McNabb and Foster equations [5]. In this particular study, the code MHIMS [6, 7, 8, 9] (Migration of Hydrogen Isotopes in Materials) and the code FESTIM [10, 11, 12] (Finite Element Simulation of Tritium in Materials) are used. The MHIMS code is used to render the dynamic of hydrogen isotopes retention in one dimension (1D) from the subsurface up to the bulk during both pulsed and continuous plasma. The FESTIM code takes inputs from the MHIMS simulations and is used in a two dimension (2D) geometry to render the behaviour of hydrogen isotopes during continuous plasmas in a complex multi-material components.

2. Plasma facing material model: W divertor target

2.1. Brief model description

The model that describes HI migration in the plasma facing materials is based on the McNabb and Foster equations [5]. In this model, the HI content is partitioned into two types of atoms: the mobile (interstitial) HI with the concentration c_m (m^{-3}) and the trapped HI with the concentration $c_{t,i}$ (m^{-3}) for the trapping site of type i . In the classical McNabb and Foster model, the equations governing the time and spatial variation of concentration of both types of particles are recalled here:

$$\frac{\partial c_m}{\partial t} = \vec{\nabla} \cdot \left(D(T) \vec{\nabla} c_m \right) + S - \sum_i \frac{\partial c_{t,i}}{\partial t} \quad (1)$$

$$\frac{\partial c_{t,i}}{\partial t} = \nu_{t,i}(T) c_m (n_i - c_{t,i}) - \nu_{dt,i}(T) c_{t,i} \quad (2)$$

where S ($\text{m}^{-3}\text{s}^{-1}$) is a volumetric source of HI (from the implantation). The other parameters are defined further in this section. The local HI concentration (m^{-3}) is calculated as $c_{\text{HI}} = c_m + \sum_i c_{t,i}$. A Fickian diffusion is assumed for the mobile particles (first term on the right hand side of equation 1), which is characterised by the diffusion coefficient of HI in the material $D(T)$ (m^2s^{-1}). The ones used in this study are reported in [11] for W, Cu and CuCrZr. Since the simulated plasma is composed of D atoms, the diffusion coefficient in each material is scaled by $1/\sqrt{2}$ [13].

The mobile interstitial HI atoms can interact with different types of defects and become trapped HI atoms. Each defect kind i has a concentration n_i (m^{-3}). According to several atomic-scale simulations, defects such as monovacancies [14, 15] or vacancy clusters [16] can retain several HIs with binding energies depending on the quantity of HI in the defects. These calculations led to a modification of the equation 2 of the classical model to take into account this multi-trapping aspect [17, 8].

The interactions between HI and trapping sites are described by two processes: detrapping and trapping. The detrapping rate constant $\nu_{dt,i}(T)$ (s^{-1}) (second term of the right hand side of equation 2) is given by:

$$\nu_{dt,i}(T) = \nu_{0,dt,i} \exp \left(-\frac{E_{dt,i}}{k_B T} \right) \quad (3)$$

with $k_B = 8.617 \times 10^{-5} \text{ eV/K}$, the Boltzmann constant, T (K) the temperature of the material, $\nu_{0,dt,i} = 10^{13}$

s^{-1} the detrapping pre-exponential factor [14] and E_{dt} the detrapping energy (eV) which depends on the amount of H in the defect (usually, it is calculated that the detrapping energy decreases with the number of trapped H). The trapping rate constant $\nu_t(T)$ (m^3s^{-1}) (first term of the right hand side of equation 2) is given by:

$$\nu_{t,i}(T) = \nu_{0,t,i} \exp\left(-\frac{E_t}{k_B T}\right) \quad (4)$$

with $\nu_{0,t,i}$ (m^3s^{-1}) the trapping pre-exponential factor and E_t the trapping energy. Assuming immobile defects and trapping energies equal to the diffusion energy, one can obtain [18]:

$$\nu_t(T) = 4\pi(R_{t,i} + \lambda)D(T) \quad (5)$$

with $D(T)$ (m^2s^{-1}) the diffusion coefficient of HI atoms in the lattice, λ (m) the capture radius of H in interstitial sites and $R_{t,i}$ the trapping radius of the trapping site i .

2.2. Model geometry

In WEST and ITER, the divertor targets are made of plasma facing units constituted of monoblocks composed of three materials:

- (i) W as plasma facing material.
- (ii) Cu as interlayer material.
- (iii) CuCrZr alloy as material for the cooling pipes.

The geometry of such monoblock is shown in [11] and in figure 1. Its thickness is $e = 12$ mm and its width is $w = 28$ mm. On the one hand, the ions from the plasma are implanted in the first nanometres in which specific trapping processes can occur such as the formation of the super-saturated layer (SSL) [19, 20]. On the other hand, the retention in such a complex component requires a 2D geometry especially when dealing with high surface temperatures [10]. The MHIMS code which includes surface and subsurface models is well suited for simulations at the nanometre-micrometre scale, while the FESTIM code is well suited for simulations of transport in multidimensional and multi-material systems at the scale of the entire component. Thus, two sets of simulations will be performed: (i) 1D MHIMS simulations in the W part and (ii) 2D FESTIM simulations with the complete geometry of figure 1.

The MHIMS simulations are used to determine the amount of hydrogen isotopes (HI) retained in the supersaturated layers and to compare the HI retention during cycled and continuous plasma exposures. In these cases, only the W armour is simulated in 1D along the axis of symmetry of the monoblock: in that direction, the W width is 7.2 mm.

The FESTIM simulations are used to determine

the total retention in the monoblocks, the permeation flux to the coolant and the desorption from the toroidal edges of the monoblocks. The 2D geometry of the monoblock presenting an axis of symmetry, only half of the monoblock is modelled.

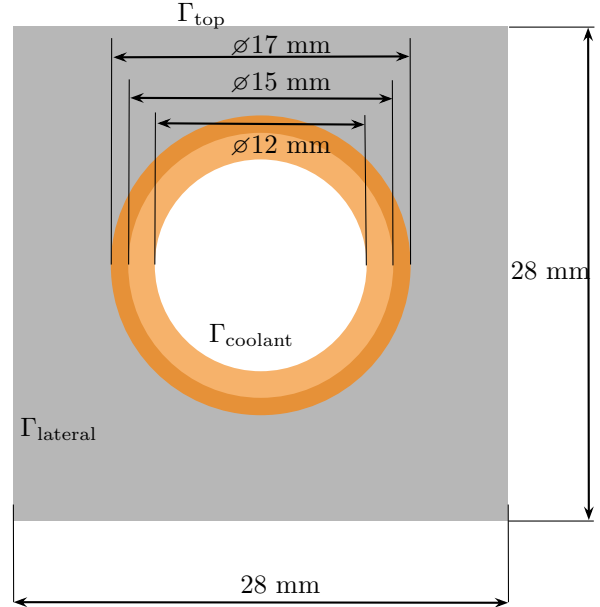


Figure 1: Monoblock geometry showing W armour ■, Cu interlayer ■, CuCrZr alloy cooling pipe ■

2.3. Simulation scenario

Three different scenarios are simulated representing different exposure conditions. The exposure parameters are shown in table 1 and correspond to an attached plasma scenario according to SOLPS simulations [1]. We consider a pure deuterium plasma so that the incident particles are deuterium atoms/ions.

Table 1 gives the incident flux of particles but the source of implanted particles has to be corrected by the reflection coefficient, r_{ion} . This reflection is estimated with the binary collision approximation (BCA) code SRIM (Stopping Range of Ions in Matter) [21]. For deuterium ion impacting a W surface with 45° with respect to the normal to the surface, the reflection coefficient is calculated to be ≈ 0.64 .

The highest energy is 115 eV, which is below the threshold for physical sputtering of W [22]. Thus, sputtering and redeposition of W surfaces atom are not accounted for in the current model. However, the kinetic energy distribution of the ions impacting the surfaces may not be mono-energetic and ions with kinetic energy above the sputtering threshold may interact with the surfaces of the plasma facing components, leading to sputtering and redeposition. The impact of sputtering and redeposition on the fuel retention estimation

Table 1: Exposure conditions for the different scenarios considered during the steady-state plasma (SSP): $\phi_{\text{heat}}^{\text{SSP}}$ (MWm^{-2}), $\phi_{\text{ion}}^{\text{SSP}}$ ($\text{m}^{-2}\text{s}^{-1}$), $E_{\text{ion}}^{\text{SSP}}$ (eV), the surface temperature $T_{\text{surf}}^{\text{SSP}}$ (K) and the temperature at the rear of the W armour $T_{\text{rear}}^{\text{SSP}}$. The surface temperature $T_{\text{surf}}^{\text{SSP}}$ resulting of such exposition is calculated using the formula in [11].

scenario	$\phi_{\text{heat}}^{\text{SSP}}$	$\phi_{\text{ion}}^{\text{SSP}}$	$E_{\text{ions}}^{\text{SSP}}$	$T_{\text{surf}}^{\text{SSP}}$	$T_{\text{rear}}^{\text{SSP}}$
I	10 MWm^{-2}	$5.0 \times 10^{23} \text{ m}^{-2}\text{s}^{-1}$	115 eV	1456 K	552 K
II	5 MWm^{-2}	$3.5 \times 10^{23} \text{ m}^{-2}\text{s}^{-1}$	75 eV	870 K	436 K
III	1 MWm^{-2}	$1.0 \times 10^{23} \text{ m}^{-2}\text{s}^{-1}$	50 eV	435 K	347 K

is discussed in more details in section 4.2. Also, it could be possible that the W surface inside the vessel is slightly covered with a native oxide layer, source of trapping sites. Such a oxide layer is not modelled here as one can consider it is sputtered by the D ions, even at 50 eV.

The surface temperature is calculated using the equation (8) in [11]: $T_{\text{surf}} = 1.1 \times 10^{-4} \phi_{\text{heat}} + 323 \text{ K}$ with ϕ_{heat} the heat flux (Wm^{-2}). The temperature field is computed using the heat transport parameters that can also be found in [11].

In the 1D-MHIMS simulations, two types of exposure are simulated:

- Cycled plasma: each cycle lasts 1,600 s with a 100 s plasma ramp-up, a 400 s steady-state plasma (SSP), a 100 s plasma ramp-down and a 1,000 s waiting phase before the next cycle. 25 cycles are simulated so that the duration of steady-state plasmas corresponds to 10,000 seconds. During the ramp-up/down, the incident energy, implantation flux and temperatures (table 1) evolve linearly up to/from their steady-state values from/to its initial values (figure 2).
- Continuous plasma: the exposure conditions in table 1 are kept constant for 10,000 s.

During the plasma exposure of the different scenarios, the temperatures at the rear of the 7.2-mm-thick W armour are taken from the FESTIM thermal module and are 552 K, 436 K and 347 K for the scenario I, II and III respectively. In the 2D-FESTIM simulations, only a 10,000 s continuous plasma is simulated.

The implanted particles coming from the plasma act as a volumetric source of mobile particles deposited in the implantation zone. It can be simulated by S in the right hand side of equation 1 with $S = f(x)(1 - r_{\text{ion}})\phi_{\text{ion}}$. The implantation profile $f(x)$ (in m^{-1}) gives the distribution of ions/atoms once they have lost all their kinetic energy to the target through collisions to the atoms (nuclear stopping power) or friction with the electronic cloud (electronic stopping power). At that point, the particles start diffusing with a Fickian diffusion, which is handled by the current

model. Thus, $f(x)$ is calculated using BCA methods as for the reflection coefficient, which can take into account the various energy dissipation processes (nuclear and electronic stopping power) that leads to stopping of ions in the metal. For the incident energies used here (table 1), the implantation zones $f(x)$ do not extent further than 10 nm below the surface. In 1D MHIMS simulations, it is possible to handle such volumetric source and the HI transport in the millimetre scale using a 500-cells mesh refined at the plasma exposed side. However, such a refinement in a 2D geometry is more problematic if one wants to stay in reasonable computation time. Thus, we decided to first simulate the exposure with the 1D MHIMS simulations and a volumetric source. Then, the results (see section 2.5) of these simulations are provided as input of 2D FESTIM simulations to determine the full D concentration field in the 2D. For scenarios I and II for which the temperatures are high, the deep migration at the millimetre-scale requires the use of the full geometry of the monoblock (half considering the symmetry) with a mesh of $\approx 60,000$ -elements. For scenario III, the HI migration does not extend deep in the bulk and only the top 0.5 millimetre are simulated as the simulation of the rest of the component is not necessary (see section 3).

2.4. Trapping parameters

2.4.1. in the subsurface: supersaturated layer It has been shown experimentally that when HIs are implanted in W with high fluxes at low temperature, even below the displacement threshold energy, the formation of a so-called super-saturated layer (SSL) can be observed. In the SSL, the concentration of H atoms can reach about 0.01 - 0.1 atomic fraction (at.fr.) in the implantation zone (up to 10 nm) [23, 19, 20]. The formation of the SSL is theoretically understood as the formation of mono-vacancies by the introduction of a large quantity of hydrogen in interstitial position, while it is energetically more favourable for the implanted H to sit in vacancies [24]. This SSL is only formed in the

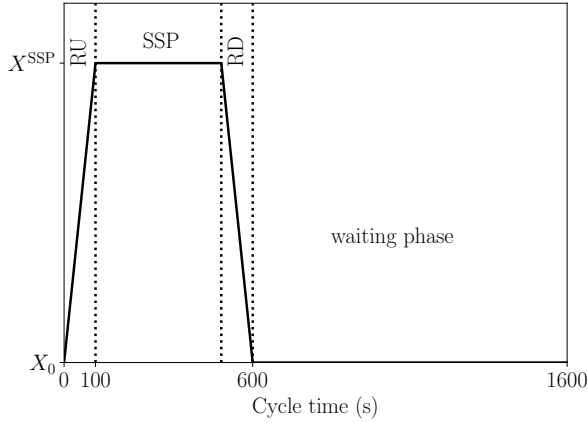


Figure 2: Evolution of the quantity X (ϕ_{ion} , E_{ion} , T_{surf}) during a 1600-seconds cycle, from its lowest value X_0 during the waiting phase to its highest value during the steady-state plasma (SSP). RU = Ramp-up, RD = Ramp-down.

implantation zone of the ions where the ions transfer their energy to the lattice. The explanation proposed in [24] and [20] is that the implantation zone is the only place where the kinetic barriers can be overcome to reach the thermodynamic equilibrium.

According to the model described in [24], the SSL formation is conditioned upon the exposure conditions (temperature and incident flux of hydrogen). According to this model, only scenario III would lead to the growth and stabilisation of the SSL (low temperature and high flux). For scenarios I and II, the temperature is too high. However, one can consider that the SSL can still be present either thanks to the previous plasma pulses or thanks to the ramp-up/down phase during which the conditions to form the SSL are met.

The trapping parameters, i.e. the detrapping energies, E_{dt} of HI from the mono-vacancies and the trapping radius R_t are given in table 2. Several DFT calculations are available for the binding of HI atoms with a mono-vacancy in W [14, 15, 16, 25]. All these studies agree on the fact that the detrapping of HI from a mono-vacancy ranges from about 0.8 eV for six trapped HI atoms to 1.5 eV for one trapped HI atom. In this work, the detrapping energies calculated by Fernandez et al. [14] are chosen to describe the energetic of HI trapping in mono-vacancies.

In the current model, mono-vacancies are assumed to have constant density with time, restricted to the implantation zone (i.e. up to 10 nm). Their concentration in the SSL is set to 5×10^{-3} at.fr. ($3.2 \times 10^{26} \text{ m}^{-3}$). Thus, once filled with 6 HI, the HI concentration in the SSL reaches $\approx 3 \times 10^{-2}$ at.fr. ($1.9 \times 10^{27} \text{ m}^{-3}$) as observed experimentally.

Table 2: Trapping parameters for the SSL: detrapping energies E_{dt} (eV) and capture radius R_t (nm). The detrapping energies are of HI from mono-vacancies are directly taken from [14].

The trapping radius is calculated as:

$$R_t(V_m) = a \left(\frac{\sqrt{3}}{4} + \left(\frac{3m}{8\pi} \right)^{\frac{1}{3}} - \left(\frac{3}{8\pi} \right)^{\frac{1}{3}} \right) [26].$$

with $a = 316$ pm, the W lattice constant.

V_1D_n	E_{dt}	R_t
V_1D_1	1.43 eV	
V_1D_2	1.42 eV	
V_1D_3	1.25 eV	0.137 nm
V_1D_4	1.17 eV	
V_1D_5	1.11 eV	
V_1D_6	0.86 eV	

2.4.2. *In the bulk* In the W armour, in addition to the SSL traps, we add two intrinsic traps with detrapping energies of 0.85 eV and 1.00 eV which have proven to be good trapping parameters to describe the bulk defects of polycrystalline W [6]. A detrapping energy of 0.85 eV can be attributed to dislocation lines [27] or metallic impurities like Fe, Ni or Cu [28]. A detrapping energy of 1.00 eV can be attributed to grain boundaries (GB) [29, 30]. The GB used in the calculations of these references are symmetrical because they were obtained with periodic DFT codes. A more realistic energetic representation of GBs would be a continuous distribution function of activation energies as mentioned in [31], where H trapping at random GB in nanocrystalline W is studied with molecular dynamics (with a bond order potential [32]). Such type of continuous distribution of detrapping energies is not yet implemented in the model and we used instead the detrapping energy that allows reproducing experimental TDS measurements. The trapping parameters for these intrinsic traps are reported in 3. Their capture radii are set to be λ and their concentration to 10^{-4} at.fr..

For the 2D FESTIM simulations, HI may reach the cooling system and permeate through W, Cu and CuCrZr. The transport and trapping parameters for Cu and CuCrZr used for these simulations are the same as the one given in [11]. At material interfaces, the conservation of the chemical potential is guaranteed with the model described in [12]. This interface model required the solubility of HIs in the different materials taken from this same reference.

2.5. Boundary conditions

For the 1D MHIMS simulations, the boundary conditions (BC) for the mobile particle concentration

Table 3: Trapping parameters for the intrinsic traps: detrapping energies E_{dt} (eV), trap concentration (n_i) and capture radius R_t (nm). The trap concentrations are expressed given in m^{-3} and also in atomic fraction, i.e. normalised to the tungsten concentration: $\rho_W = 6.338 \times 10^{28} m^{-3}$.

E_{dt}	n_i	R_t	defect type
0.85 eV	$6.338 \times 10^{24} m^{-3}$ (10^{-4} at.fr.)	λ	Dislocations, Metallic impurities [27, 28]
1.00 eV	$6.338 \times 10^{24} m^{-3}$ (10^{-4} at.fr.)	λ	Grain boundaries (GB) [29]

are:

- (i) On the plasma facing surface, a Dirichlet condition: $c_m(0, t) = 0$. It represents an instantaneous desorption of all particles arriving at the surface.
- (ii) On the rear side of the W armour, a Dirichlet condition: $c_m(7.2 \text{ mm}, t) = 0$.

The BC for the rear side of the W armour is the closest conditions one can use with MHIMS to simulate a realistic permeation behaviour of HIs in the W armour.

For the 2D FESTIM simulations in the semi-monoblock, the BC for the mobile particle concentration are:

- (i) On the plasma facing surface (Γ_{top} , a Dirichlet condition: $c_m = c_m^{MHIMS}(X_{imp})$. With X_{imp} being the implantation depth of the HI atoms.
- (ii) On the surface of the cooling pipe ($\Gamma_{coolant}$, a condition based on a recombination coefficient: $-D_{CuCrZr} \nabla c_m \cdot \vec{n} = K_{rec} c_m^2$ with D_{CuCrZr} ($m^2 s^{-1}$) the diffusion coefficient of HI in CuCrZr, K_{rec} ($m^4 s^{-1}$) the recombination coefficient taken from [11] and \vec{n} the normal to the surface.
- (iii) On the right side of the semi-monoblock, a homogeneous Neumann condition: $\nabla c_m \cdot \vec{n} = 0$ to account for symmetry conditions.
- (iv) On the left side of the semi-monoblock ($\Gamma_{lateral}$), a Dirichlet condition: $c_m = 0$ that simulates the desorption of HI from the toroidal edges of the monoblock, in the toroidal gap.

For a given scenario, first, MHIMS calculates the concentration of mobile HI in the implantation zone, $c_m^{MHIMS}(X_{imp})$ with the ions coming from the plasma being treated as a volumetric source for the different scenario. Then, FESTIM uses this calculated concentration as an input to calculate the D concentration field in the 2D geometry of the monoblock.

3. Simulations Results

3.1. 1D simulations

First, we present the results of the MHIMS simulations especially the impact of simulating cycled (with the evolution given in figure 2) or continuous plasma.

3.1.1. D depth profile Figure 3 shows the evolution of the D depth profile in the 7.2 mm W armour after 5 - 25 cycles for scenario I (a), II (b) and III (c). The depth profile just before the ramp-down phase (end of the steady-state plasma) is also shown (black dashed lines). The D depth profiles are similar in scenarios I and II after the end of the cycles: a high concentration in the SSL area (5-10 nm) with about $10^{27} D/m^{-3}$, a second step up to 10 μm with about $10^{25} D/m^{-3}$ accompanied by a tail up to 1 mm and the bulk part. The D depth profiles for scenario III only exhibit two features: the high concentration in the SSL and the step of constant concentration up to the migration depth, which after 25 cycles is around 400 μm .

There is a big difference between the depth profiles before the ramp down (black dashed lines) and at the end of the cycles for scenarios I and II. This is explained by the retention during the 100 seconds of plasma ramp-down during which the temperature decreases while the incident flux is not zero: trapping takes over detrapping increasing the filling ratio of the traps. Such ramp-down retention has already been briefly described in [10] and it will be investigated further in the following. It is also important to note that the quantity of D retained during this part of the plasma is independent of the cycles as one cannot distinguish the D profiles in this first mm.

The difference between the cycles is observed in the bulk part of the depth profile which shows the migration further and further in the bulk as the number of cycles increases. In addition, for scenarios I and II, the D concentration tends to increase close to the rear part of the W where the temperature is cooler than at the front exposed to the plasma.

Even though the retention in the SSL after the ramp down is similar for the three scenarios, it is different during the steady-state plasma (black dashed lines in figure 3). In Scenario III, the vacancies in the SSL are almost exclusively (99%) filled with 6 D during the steady state plasma. In scenario II, there are mostly VD_2 (42%), VD_3 (32%) and VD_4 (15%) with a few percents of empty vacancies. In scenario I, there are almost only empty vacancies (99%). Thus, during scenarios II and III, since most of the vacancies are filled with at least 1 D, the structure of the defects in

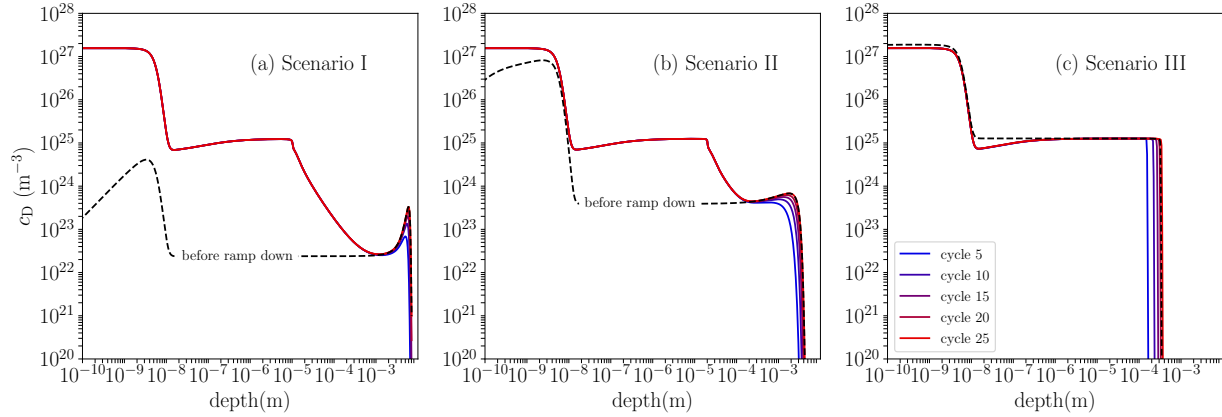


Figure 3: Results of the MHIMS simulations: Concentration of D in the W armour after 5 - 25 cycles of 1,600 seconds with the exposure conditions of scenario I (a), scenario II (b) and scenario III (c). The concentration of D before the ramp down of cycle 25 is also shown in black dash line.

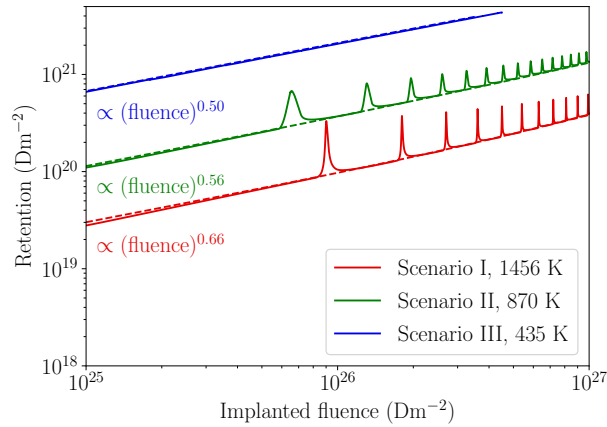


Figure 4: Evolution of the D retention in the 7.2 mm W armour after 10,000 seconds of steady-state continuous plasma (dashed lines) or after 25 cycles (solid line). The retention is shown as a function of the implanted fluence to be able to compare continuous and cycles exposures.

this SSL should not change that much as the presence of D inhibits the migration [14] and thus coalescence of vacancies. For scenario II, the few percents of empty mono-vacancies could possibly move and aggregate with filled vacancies as shown in [33]. For scenario I, almost all vacancies are empty and one could expect them to eventually be annealed following the various annealing steps reported experimentally in [34, 35]. According to Zibrov et al. [35], the SSL would actually disappear at 1456 K during the steady-state plasma but could be reconstructed during the ramp-down as the temperature decreases.

3.1.2. cycle vs continuous plasma: D retention Figure 4 shows the evolution of the D retention for the various scenarios and for cycled (solid line) and continuous (dashed line) exposures as a function of the implanted fluence. The spikes appearing periodically on the retention for scenarios I and II are the retention occurring during the ramp down phase which is removed during the next ramp-up phase. When focusing only on the evolution of the retention between these spikes, i.e. during the steady-state plasma, no obvious differences can be observed between cycled and continuous plasma, at least in the time dynamics: the retention due to the migration of D deeper and deeper in the bulk is the same regardless if the plasmas are cycled or not. Thus, the study of D retention and permeation for long exposure times can be studied with either types of plasma exposures.

The evolution of the retention has been interpolated using the curve_fit function of the python package scipy [36, 37] with a power law. For scenario III, the exponent of the power law is 0.5 showing a retention limited by the migration in the bulk. And as the surface temperature increases, the exponent deviates from 0.5 to reach 0.66. This effect is explained by the lower temperature at the rear side of the W armour which tends to increase the concentration in this area. In [38], we already showed an evolution of the exponent but it was going below 0.5. We were looking at the evolution of the retention at the end of the cycle which accounts for the retention during the ramp-down which is not taken into account in figure 4. This is because we were not taking the evolution of the retention only during the steady-state plasma but we were accounting for the retention during the ramp-down. Doing so with the present data would also make the retention evolve with a power law below 0.5. However, if one wants the

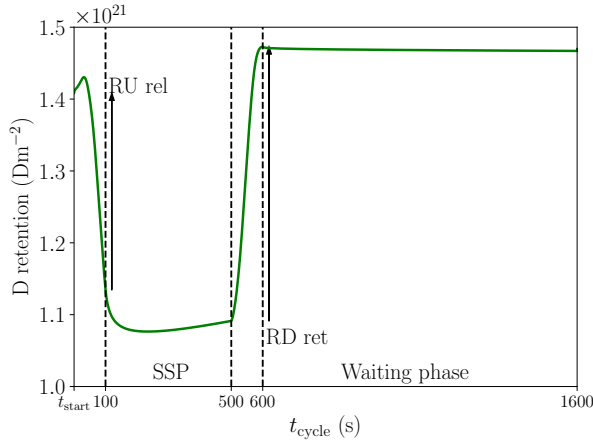


Figure 5: Evolution of the D retention with time during the 10th cycle of scenario II ($T_{\text{surf}}^{\text{SSP}} = 870$ K). The beginning/end of the plasma ramp-up/down are marked with vertical dashed line and the retention released during the ramp-up (RU rel) and retained during the ramp down (RD ret) are marked with arrow.

exponent to make sense with the bulk migration dynamic, one should focus only on the retention during the steady-state plasma.

3.1.3. Ramp-down retention/Ramp-up release Figure 5 shows the evolution of the D retention during the 10th cycle of scenario II. During the ramp down phase (first 100 seconds), the retention decreases drastically due to the temperature increase. This leads to a release during the ramp down highlighted by the arrow *RU rel* in figure 5. During the steady-state plasma, the retention keeps decreasing in the next 100 seconds before increasing again. When the plasma ramp down starts, the retention goes up during the ramp down which is highlighted by the arrow *RD ret* in figure 5. This increase of the D retention appears because the PFC is actively cooled: the particle flux and the temperature decreases with the same behaviour (figure 2), and eventually the temperature is low enough and the flux of particle is still high enough to favour trapping over de-trapping. If the fluxes were immediately zero after the steady state plasma or if the temperature decreased much slower than the flux (inertial PFC for instance), no ramp down retention would be observed. Figure 6 reports the quantity of D released/retained during the ramp-up/down in the three scenarios. These quantities are computed as shown on figure 5 (see the arrows). No release during the ramp-up is reported for the first cycle as the material is empty at the beginning of the simulation: for any scenario, it would be negative (uptake of D) and would not add anything significant to the interpretation of the dynamic of the D retention.

For scenario III, the retention during the ramp

down tends to decrease and the release during the ramp-up is negative meaning there is an uptake of D during this phase. This behaviour is expected for a cold scenario with small variations of temperature.

For scenarios I and II, the retention during the ramp down is positive as well as the release during the ramp-up. In addition, both are very close, the difference being that during the first 100 seconds of the steady-state plasma, the retention keeps decreasing (see figure 5). Thus, the retention during the ramp down phase, localised close to the exposed surface of the PFC, is removed during the ramp-up phase, as explained in the previous section. This dynamic retention stays constant of the order of 10^{20} Dm^{-2} during all cycles and may act as a source of fuel for the plasma during the ramp down.

The WEST divertor is composed of 480 PFUs and assuming there are two monoblocks per PFU exposed to scenarios I and II (outer and inner), one can estimate that the dynamic retention during the ramp-up/down represents about 2×10^{20} D atoms. Taking a WEST plasma of 15 m^3 and a plasma density of $9 \times 10^{19} \text{ m}^{-3}$ (high power scenario in [39]), the retention/release during the ramp down/up represents about 15% of the total amount of D in the plasma. The ITER divertor is composed of 54 cassettes with 16 PFUs on the inner side and 22 PFUs on the outer sides. Assuming there is one monoblock per PFU exposed to scenarios I and II, the total quantity of D retained/released during the ramp down/up is of the order of 4×10^{20} D atoms. Taking an ITER plasma of 830 m^3 with a density of 10^{20} m^{-3} , the retention/release during the ramp down/up represents 0.5% of the total amount of D in the plasma. Thus, this retention and release could be a possible issue for the control of the source of fuel during the plasma ramp up especially in smaller tokamaks. Indeed, currently, there is no direct coupling between plasma transport codes such as SOLPS [40, 41] or SOLEDGE3X-EIRENE [42, 43] and retention codes like the ones used here. Thus, no ionisation of the emitted particles is taken into account in the retention code, that would eventually increase the local plasma density and possibly affect the exposure conditions. However, first attempts to calculate recycling coefficient with retention codes have emerged [44] with the goal of coupling SOLEDGE3X-EIRENE and the Desorption from Wall ElemEnts (D-WEE) module, which contains MHIMS to model the HI/material interactions.

It is important to note that the quantity given here are indicative and would likely change with the width of the heat/particle deposition on the divertor or with the duration of the ramp-up/down. For instance, a shorter ramp down may reduce the retention during the ramp down. On the contrary, a wider deposition

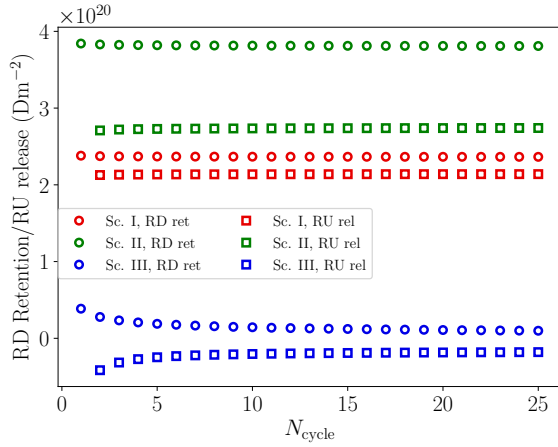


Figure 6: Quantity of D retained during the ramp down (RD) and released during the ramp-up (RU) phases as a function of the number of cycles N_{cycle} for the different scenarios.

of the fluxes on the divertor would increase the overall quantity of D retained during the ramp down.

3.2. 2D simulations

The concentration of mobile particles, $c_m^{\text{MHIMS}}(X_{\text{imp}})$, calculated in the 1D MHIMS and given as input to FESTIM are reported in table 4. In the MHIMS simulations, the concentration of mobile particles reached 95% of the value reported in table 4 in less than a second. Thus, a constant concentration is chosen as input of the FESTIM simulations. One can see that the concentration of mobile D is higher for the coldest scenario. Indeed, the mobility of D is related to (i) the gradient of the concentration of mobile particles (i.e. to ϕ_{inc} , and E_{inc}) and (ii) the diffusion coefficient (i.e. the temperature T_{surf}). This is calculated by the model with a volumetric implantation source (with MHIMS) and given as an input to FESTIM. However, one can estimate the concentration of mobile particles for a given set of exposure conditions assuming no (or negligible) gradient to the bulk and a full recycling of implanted D [11, 20, 24]: $c_m = \frac{(1-r_{\text{ion}})\phi_{\text{inc}}R_{\text{imp}}}{D(T)}$ with R_{imp} (m) the implantation depth of the ions. Since (i) from scenario I to III the diffusion coefficient $D(T)$ drops by 42, and (ii) the incident flux ϕ_{inc} and the implantation depth R_{imp} only decrease by 5 and 1.6 respectively, the above assumption on c_m leads to a 5 time higher concentration of mobile particles for scenario III.

The conclusion of the previous sections concerning the retention, migration and permeation in the far bulk is that one can simulate either continuous or cycled plasma exposures without changing the results. The continuous plasma are much faster to run than cycled

Table 4: Output value of $c_m^{\text{MHIMS}}(X_{\text{imp}})$ given as input to the 2D FESTIM simulations. This is the local concentration of mobile particles in the implantation zone.

scenario	$c_m^{\text{MHIMS}}(X_{\text{imp}})$ (m^{-3})
I	2.01×10^{22}
II	3.20×10^{22}
III	9.74×10^{22}

plasma with FESTIM so we decided to run 10,000 seconds continuous plasma exposures. First, the 2D D retention fields after 10,000 seconds of exposure are presented and then macroscopic data are extracted from the simulations.

3.2.1. 2D retention fields Figure 7 shows the deuterium retention in the half-monoblock after 10,000 seconds of plasma exposure for scenario I (a) and II (b). As already mentioned in [10, 11, 12], and as observed in the 1D depth profiles (figure 3), the presence of the thermal gradient implies that the maximum of D concentration is not at the exposed surface but near the cooling pipe. This is especially visible for scenario I (hottest scenario) for which the maximum of retention tends to follow the shape of the cooling pipes. The impact of the interface model is not seen on the D concentration of scenario II but it is seen for scenario I. The continuity of the chemical potential chosen here leads to a discontinuity of the concentration of mobile particles at the W/Cu and Cu/CuCrZr interfaces. Especially, as shown in [12], this tends to enhance the retention in the CuCrZr part.

According to the 1D simulations, the D migration depth does not exceed 500 μm for scenario III (figure 3(c)). Thus, for this scenario, simulating the D transport in the same geometry as for scenarios I and II is not necessary. Instead, we simulate a 500 $\mu\text{m} \times 14$ mm layer of W. One of the 14 mm boundary (Γ_{top}) is exposed to the plasma (Dirichlet BC see section 2.5) and D is allowed to desorb instantaneously from one of the 500 μm boundary (Γ_{lateral}). Both are Dirichlet BC as explained in see section 2.5. The temperature in this 500 $\mu\text{m} \times 14$ mm rectangle is set to be the temperature of scenario III. The resulting D retention field after a 10,000 seconds exposure is shown in figure 8 (it does not show the full 14 mm width but it is zoomed on the corner where D is allowed to desorb). As in the 1D simulations, far from the desorbing edge, the D concentration is constant up to the migration depth which is about 300 μm . However, close to the toroidal edge, the migration depth decrease, which is also seen for scenario II (figure 7(b)). This is because D is allowed

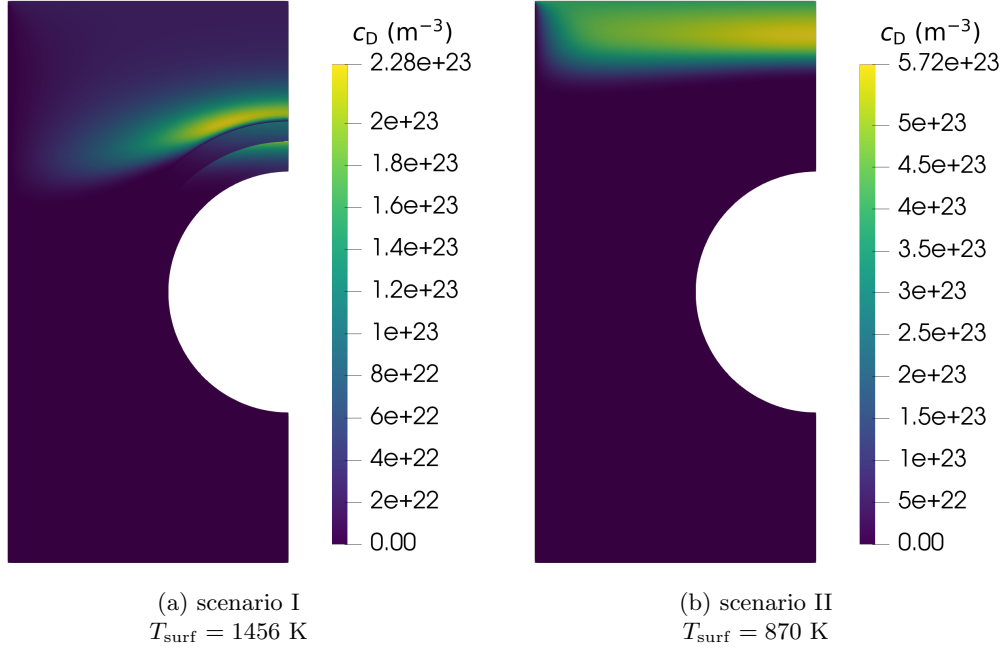


Figure 7: Results of the FESTIM simulations for scenario I (a) and II (b): deuterium retention field c_D (m^{-3}), in the semi-monoblock after 10,000 seconds of continuous. The colour bar have different scales .

to desorb instantaneously from the toroidal edge to the gap between PFUs forcing the D concentration at this edge to 0. These edges effects stay marginal if one only focuses on the D retention. However, the desorption from the toroidal edges is a source of fuel recycling from the wall to the plasma which is estimated in the next section.

3.3. Macroscopic quantities

3.3.1. D inventory The total D inventory in one monoblock exposed to scenario I, II or III can be calculated as:

$$I_D = 2eR_D^{\text{FESTIM}} + ewR_D^{\text{SSL,MHIMS}} \quad (6)$$

where R_D^{FESTIM} (Dm^{-1}) is the retention computed by FESTIM in the 2D geometry which accounts for the intrinsic traps and the mobile particles. $R_D^{\text{SSL,MHIMS}}$ (Dm^{-2}) is the retention computed by MHIMS in 1D in the SSL only, as the mobile particles and the HI trapped in the intrinsic traps are already taken into account in R_D^{FESTIM} . The SSL is very close to the surface (10 nm) and the retention in it is not influenced (or only marginally) by the 2D shape of the monoblock. Thus, we used the linear combination of equation 6 to calculate the D retention.

This quantity is shown in figure 9 for the three scenarios during a continuous 10,000 seconds plasma

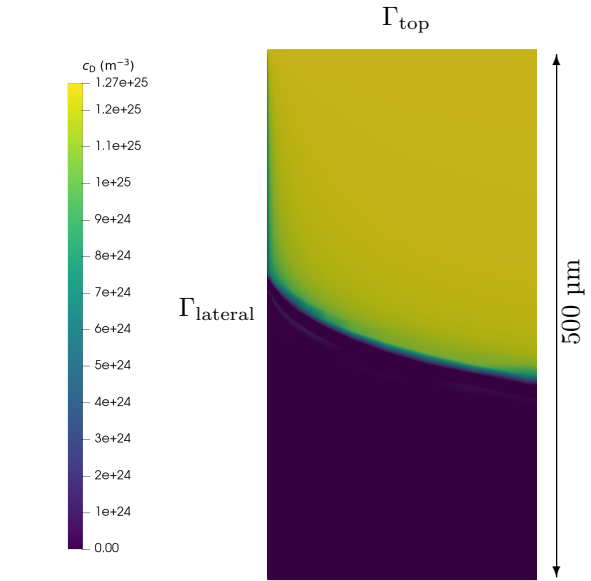


Figure 8: Results of the FESTIM simulation for the scenario III: deuterium retention field c_D (m^{-3}) after 10,000 second of continuous plasma exposure (on Γ_{top}). The thickness of the simulated material is 500 μm . The width is the same as for the other scenarios (14 mm) but for sake of clarity, the figure is zoomed in the corner from which the D is allow to desorb (Γ_{lateral}). The temperature is 435 K.

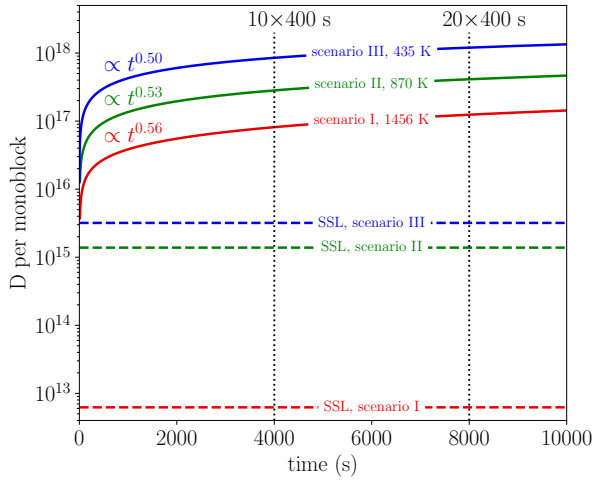


Figure 9: D retention per monoblock I_D for the three simulated scenario during a continuous 10,000 s plasma exposure. The contribution of the SSL retention is also shown with the dashed line.

exposure in addition to the SSL contribution to the SSL. The SSL contribution does not evolve during the continuous exposure: the SSL is located in the first 10 nm below the surface and is almost instantaneously saturated. For scenario II and III, this contribution is $> 10^{15}$ D per monoblock ($\approx 10^{18-19}$ Dm^{-2}) and represent few % of the total inventory at the beginning of the simulations but becomes rapidly negligible on the total inventory. It is however important to assess the content of D in the SSL as it is a close source of fuel and transient like ELMs could modify that content [33] and perturb the recycling from the wall to the plasma [45]. For scenario I, the content of D in the SSL is completely negligible compared to the retention in the bulk which is expected considering the high temperature in this scenario.

Despite the much lower migration depth, the inventory is maximum for the lowest temperature. This is consistent with previous simulation work in 1D [38, 46] and 2D [11] geometry. The evolution of the retention has also been fit with power laws. For scenario III, the retention evolves as a square root of time which agrees well with the steady-state model presented in [7] for migration limited bulk retention. For scenario I and II, the power law slightly deviates from the square root of time as shown on figure 4. However, the exponent obtained from the 1D simulations is further away from the square root of time than the one obtained from the 2D simulations which is explained by the 2D complex migration of D around the cooling pipe, especially in scenario I (figure 7(a)).

3.3.2. Permeation flux to the coolant Figure 7(a) shows that D reached the CuCrZr pipes in 10,000 seconds. It leads to permeation of D from the plasma facing side to the cooling system creating a leak of D which is shown in figure 10(a). This permeation is observed only for the simulation of scenario I with the hottest temperature. After 10,000 seconds of continuous plasma, the quantity that is released to the water cooling system is calculated to be 1.35×10^{14} D per monoblock with a flux $\approx 0.6 \times 10^{11}$ D/s per monoblock. This flux is still growing as the exposure time showing the same transient form as in [12] in which the permeation flux eventually stabilizes (at least for the 1D simulations). Thus, one could expect that the permeation flux would eventually reach a steady-state, though the retention is still growing after 10^7 seconds of plasma exposure in [12] making the time to reach the steady-state far beyond our simulation time scale.

In section 3.1.3 we assumed that one monoblock per PFU would be exposed to scenario I at the outer and inner targets: the total quantity released to the cooling system after 10,000 seconds is 2.8×10^{17} D atoms and a permeation flux 1.2×10^{14} D/s. If one extend these results to the ITER nuclear phase during which the plasma is a half deuterium/half tritium mixture, it means the permeation flux to the cooling system after 10,000 seconds of continuous exposure is estimated to 0.1 MBq/s (50 Bq/s per monoblock) for a total of 252 MBq after 10,000 seconds of continuous plasma. This would require tritium removal from the cooling system, if the monoblocks are exposed to such a high temperature for more than 10,000 seconds in total. It is important to note that the interface model assume perfection of the interfaces between both material: there is no traps which slows down the permeation processes. The impact of trap at the interface may be significant if the trap is energetically deep as shown in the appendix of [12] but it requires a parametrisation which is not yet available. The values given here is thus an upper limit for the permeation flux.

3.3.3. Outgassing at the toroidal edge Figure 7 and figure 8 show that the D retention field is affected by the desorption from the toroidal edge of the monoblock Γ_{lateral} . The desorption flux from these edges to the gap between monoblocks is calculated as $2e \int_{\Gamma_{\text{lateral}}} (-D(T) \nabla c_m \cdot \vec{n}) dl$ and shown in figure 10(b) for the three scenarios. The growth seems to have two time constants: a fast one which contributes to the most of the desorption flux, and a slower one with a much smaller contribution. It means that most of the desorbed D is done at the upper corner of the toroidal edge (fast time constants) and the slow time constant is due to the slow migration in the bulk. The

former process has a smaller contribution as D migrates toward colder area where $D(T)$ and thus the desorption flux is smaller (and the gradient of mobile particle is lower as well).

The formula for the desorption flux implies that the desorption flux is basically driven by the value of the gradient of c_m , hence by the value of $c_m^{\text{MHIMS}}(X_{\text{imp}})$ (table 4) and by the value of the diffusion coefficient, hence the temperature. A first crude assumption would then mean the desorbing flux is proportional to $\propto D(T_{\text{surf}})c_m^{\text{MHIMS}}(X_{\text{imp}})$ which is validated by the ratio between the desorbing flux of the three scenario: the desorbing flux of scenario I is twice the desorbing flux of scenario II and 10 times the scenario of scenario III.

Considering that one monoblock per inner/outer PFU target is exposed to each of these scenarios, the total quantity of D desorbing from the toroidal edges is 1.55×10^{17} D/s (5.8×10^{-4} Pa.m³.s⁻¹) for the WEST divertor and 3.32×10^{17} D/s (1.2×10^{-3} Pa.m³.s⁻¹) for ITER. This amount is very low (2 order of magnitude below the implanted flux on the top surface of the monoblock) thus, the desorption from the toroidal edges is negligible with respect to the desorption from the front surface. We simulate a 2D geometry: no poloidal edges are simulated and it should be another source of desorption from the monoblocks, but still very moderate.

4. Discussion

4.1. Permeation short cut through the poloidal gaps

Zhou *et al* [47] showed experimentally that HI atoms can penetrate in the gaps between adjacent monoblock in the poloidal direction. In these gaps, HI are directly in contact with the CuCrZr cooling pipe, thus offering a short cut for HI to reach the cooling system. An estimate of tens of seconds was given in [47], which is much faster than the thousands of seconds required for HI to diffuse across the full monoblock as shown in figure 10 (a). However, a proper estimate of the quantity of HI reaching the coolant via that channel would require the knowledge of the gas pressure and/or the plasma density of HI in these gaps. Such estimate is not easy to do since HIs come from two different sources: (i) from the plasma penetrating the gaps, and (ii) from the HIs desorbing from the poloidal edges of the monoblocks. In principle, the former (i) can be determined by plasma transport and gas kinetic models, while the latter (ii) required 3D FESTIM simulations of H transport and desorption in the monoblocks. In addition, 3D simulations of the monoblock plus cooling pipe are also required to calculate the permeation flux to the cooling pipe coming from both the gap short cut and the monoblock. Due to the complexity of

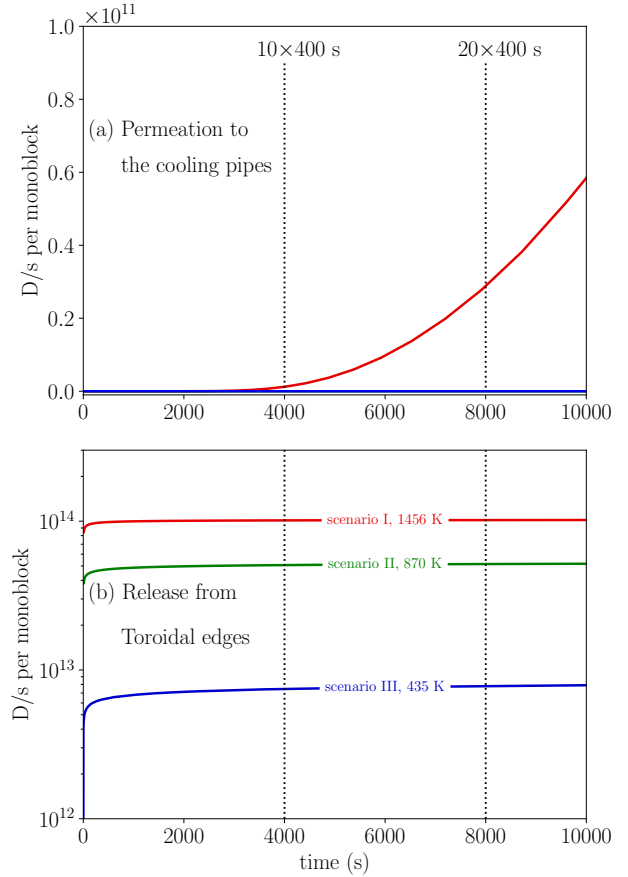


Figure 10: D release to the cooling pipes(a) and from the toroidal edges (b) extracted from the 2D-FESTIM simulations for scenario I, II and III. For scenario II and III, the release to the cooling pipes (permeation flux) is 0 and both curves overlap each other.

such simulations, and given the uncertainty of the HIs flux via the short cut, we here focus on the best case scenario regarding the HI permeation time scale to the coolant and we leave the above mentioned simulations for another complete work.

4.2. Impact of the sputtering/redeposition on the HI retention

The highest energy considered is 115 eV which is below the threshold for physical sputtering of W according to [22]. However, in an edge plasma, the particles are not mono-energetic: there is a distribution given by the ionic temperature. Thus, the incident energies of the particles hitting the wall are given by this distribution affected by the presence of the magnetic sheath (that tends to accelerate the ions). One can expect to have some fast ions that may sputter the W armor, though at a very low rate (3×10^{-4} atoms per incoming ions according to [22]). To take into account this effect, one

could use a similar workflow as described in [48] that gives a ionic temperature to a plasma sheath code to obtain the distribution of the ion energy on the wall. Then, a binary collision approximation (BCA) model and an impurity transport model are used to estimate the erosion and redeposition rates. The results presented in [48] suggest the presence of an erosion zone around the strike point (due to the He ions produced by the fusion reactions) and some of these sputtered W atoms are redeposited toward the private flux region. This erosion/redeposition may affect the retention calculated in this study, especially in the sub-surface region and the SSL.

Scenario I and II would most likely be representative of erosion zones (being at or close to the strike point). The exposure conditions of these scenarios do not allow the formation of the SSL [24] (too high temperature) but we still assumed such SSL can be present due to past exposure (ramp up/down phases or colder irradiation conditions). Thus, if these scenarios are in an erosion zone, the SSL would be progressively removed without any possibility to be rebuilt except during ramp up/down phases. Consequently, the contribution of the SSL to the total inventory (dashed line of figure 9) would disappear, knowing it is already low compared to the bulk HI inventory. For the plasma background calculated in [48], the net erosion flux is estimated to be of the order of $10^{18} \text{ m}^{-2}\text{s}^{-1}$ (0.1 monolayer per second). Taking this value as a first estimate and the thickness of 1 monolayer to be 1 Å, a plasma of 10,000 s would remove about 100 nm of material, removing completely the SSL.

Scenario III would most likely be representative of a deposition zone. For this scenario, the formation of the SSL is possible according to [24] (high flux and low temperature). The SSL is formed in the implantation zone where the energy is deposited: the SSL will only grow in the first nanometers and the SSL will build up as the material is deposited. The final quantity of HI in the SSL will be linked to a tradeoff between the SSL traps (mono-vacancies) creation rate and the material deposition rate. If the material is very rapidly deposited compared to the creation of the SSL traps, the SSL will be thick but with a low amount of HI while if the creation of the SSL traps is fast compared to the material deposition, the SSL will be thin but with a high concentration of HI.

4.3. Defects formation and evolution

4.3.1. Super-saturated layer We modelled a SSL in the sub-surface by a fixed concentration of mono-vacancies up to 10 nm. However, such a SSL is induced by D ion irradiations [19, 20] and one should include the dynamics of defect formation in the model using trap creation equation as proposed in [49, 50]. Such

model exists in MHIMS [6, 51] and have even been upgraded to account for the stabilisation of traps by the presence of trapped H [52, 53]. So far, the domain in which the SSL could be formed has been studied with thermodynamic models [14, 24, 54, 55, 56]. Qualitative explanations have been proposed to explain how the kinetic barriers to form vacancies are reached during ion implantation [19, 24, 20] but further studies are required to establish a consistent model and so far, the creation rate used in [6, 49, 50] to describe the SSL formation are ad-hoc parameters used to fit the experiments. According to the reported values, the saturation of the SSL occurs for fluence of the order of 10^{24} Dm^{-2} which is much lower than the order of magnitude of the fluences simulated in this paper. Thus, we did not use trap creation model to simulate the SSL formation in this work.

Another aspect which is not treated here is the evolution of the SSL thanks to mono defect or defect clusters migration, clustering or annihilation with other mono-vacancies or self-interstitial atoms (SIA) created in the SSL region. The binding of H with SIA is not high [15] and the trapping of H into mono-vacancies inhibits their recombination with SIA [55, 57]. Thus, due to their high mobility [26, 58], the SIA can move in the lattice, and since the SSL is very close to the surface, the SIA would most likely disappear at it. However, part of them may diffuse deeper toward the bulk, agglomerate into bigger SIA clusters which increases the binding energy of H to this type of defects [27]. An other aspect of this SSL evolution is that empty mono-vacancies can move above 500 K [34, 35]. During the steady-state of scenario I, the SSL is almost empty. The defects in the SSL could evolve and eventually form vacancy clusters containing HI [33, 35, 59]. The detrapping energies of HI from such defects are known from DFT calculations [16]. The mobility and clustering of vacancies (or traps in general) is not yet implemented in our model but one could use either kinetic Monte Carlo [26, 58] or cluster dynamics [60] methods to assess the distribution and evolution of the defects in the SSL to determine the trap concentration in this zone.

4.3.2. Thermo-mechanical induced traps During scenario I and II, the temperature at the surface of the monoblock is above the ductile-to-brittle transition temperature (DBTT) of W. Because of the thermal expansion, the temperature gradient the thermal expansion mismatch between materials, residual stress could be created in the monoblock and since it is above the DBTT, plastic deformation can take place. This plastic deformation is the source of new trapping sites like dislocations but it has also been shown that strain in the 3-38% range give birth to vacancy like

defects (jogs at dislocations) that are deep traps for HI [61]. The estimation of this effect on the HI retention in the monoblock can be addressed as in [62] by first computing the plastic strain induced by thermal fields, which is then used in the current modelling as a time and space dependent trap density. It is worth noting that the plastic strain estimation is strongly dependent on metallurgical features (dislocations, GB, grain sizes and orientations ...) that are triggered with temperature [63].

5. Conclusion

In this work, the deuterium transport in W plasma facing components of the WEST and ITER divertors is simulated. Three scenarios are simulated that are relevant for plasma operations. The surface temperatures of these scenarios are 1456 K, 870 K and 435 K which are representative of temperature at the strike-point, few cm from the strike point and far from the strike point during an attached plasma. Two types of plasma exposures are simulated: a continuous plasma exposure of 10,000 seconds and 25 cycles of 1,600 seconds with 400 seconds of steady-state plasma. Two types of simulations are run: 1D simulations in the 7.2 mm thick W armour which takes into account the super-saturated layer present in the sub-surface region and 2D simulations with the actual multi-material geometry of the components.

The 1D simulations show that there is no visible difference between the continuous and cycled plasma if one focus on the retention and migration in the bulk of the plasma facing components. This is due to moderate outgassing between discharges, which is limited by the retrapping process. The cycling introduces plasma ramp-up and ramp-down during which a dynamic retention is observed. During the ramp-down, the surface temperature decreases together with the particle flux which creates a deuterium rich layer of about 10 μm below the surface. This layer is quickly desorbed to the plasma during the following ramp-up. This dynamic retention is only visible in the hottest scenarios and is always the same independently of the cycles.

The 2D simulations are only run with the continuous plasma exposures. To speed up the simulations, the implantation is simulated with a surface concentration of mobile particles taken from the 1D simulations. From these interfaces simulations, three macroscopic quantities per monoblock are extracted: the total deuterium retention, the permeation flux to the cooling system and the desorption rate from the poloidal edge of the components. The simulations show that the retention in the super-saturated layer can reach 10^{15} D per monoblock (for the coldest exposures) but for long plasma exposure, the retention is dominated by the

bulk. However, the presence of such high quantity of D near the surface may affect the edge plasma, especially during transient. Then, as already mentioned in previous studies [11, 38, 46] despite being the scenario with the highest incident flux of particles, the hottest scenario has the lowest retention. It is also the only scenario leading to the permeation of D atoms after 10,000 seconds of exposure. Finally, it is calculated that the desorption from the toroidal edges of the components stays a negligible source of recycling depending on the morphology of the heat and particle flux on the divertor.

Acknowledgements

Centre de Calcul Intensif d'Aix-Marseille is acknowledged for granting access to its high performance computing resources. This work has been carried out within the framework of the EUROfusion Consortium and has received funding from the EURATOM research and training program 2014-2018 and 2019-2020 under grand agreement No 633053. The views and opinions expressed herein do not necessarily reflect those of the European Commission. The project leading to this publication has received funding from the French National Research Agency (Grant No. ANR-18-CE05-0012).

References

- [1] R.A. Pitts, X. Bonnin, F. Escourbiac, H. Frerichs, J.P. Gunn, T. Hirai, A.S. Kukushkin, E. Kaveeva, M.A. Miller, D. Moulton, V. Rozhansky, I. Senichenkov, E. Sytova, O. Schmitz, P.C. Stangeby, G. De Temmerman, I. Veselova, and S. Wiesen. Physics basis for the first iter tungsten divertor. *Nuclear Materials and Energy*, 20:100696, 2019.
- [2] HD Bui and S Taheri. The thorn singularity of a bimaterial solid in thermoelasto-plasticity. *COMPTEs RENDUS DE L ACADEMIE DES SCIENCES SERIE II*, 309(16):1527–1533, 1989.
- [3] M. Missirlan, J. Bucalossi, Y. Corre, F. Ferlay, M. Firdaouss, P. Garin, A. Grosman, D. Guilhem, J. Gunn, P. Languille, M. Lipa, M. Richou, and E. Tsiatroni. The west project: Current status of the iter-like tungsten divertor. *Fusion Engineering and Design*, 89(7):1048–1053, 2014. Proceedings of the 11th International Symposium on Fusion Nuclear Technology-11 (ISFNT-11) Barcelona, Spain, 15-20 September, 2013.
- [4] C. Grisolia. Plasma wall interaction during long pulse operation in tore supra. *Journal of Nuclear Materials*, 266-269:146 – 152, 1999.
- [5] A McNabb and P. K Foster. A new analysis of the diffusion of hydrogen in iron and ferritic steels. *Journal of Transaction of the Metallurgical Society of AIME*, 227:618–627, 1963.
- [6] E.A. Hodille, X. Bonnin, R. Bisson, T. Angot, C.S. Becquart, J.M. Layet, and C. Grisolia. Macroscopic rate equation modeling of trapping/detrapping of hydrogen isotopes in tungsten materials. *Journal of Nuclear Materials*, 467:424 – 431, 2015.

- [7] E.A. Hodille, A. Založnik, S. Markelj, T. Schwarz-Selinger, C.S. Becquart, R. Bisson, and C. Grisolia. Simulations of atomic deuterium exposure in self-damaged tungsten. *Nuclear Fusion*, 57(5):056002, 2017.
- [8] E A Hodille, Y Ferro, N Fernandez, C S Becquart, T Angot, J M Layet, R Bisson, and C Grisolia. Study of hydrogen isotopes behavior in tungsten by a multi trapping macroscopic rate equation model. *Physica Scripta*, T167:014011, jan 2016.
- [9] M. Pečovnik, E.A. Hodille, T. Schwarz-Selinger, C. Grisolia, and S. Markelj. New rate equation model to describe the stabilization of displacement damage by hydrogen atoms during ion irradiation in tungsten. *Nuclear Fusion*, 60(3):036024, feb 2020.
- [10] Rémi Delaporte-Mathurin, Etienne A. Hodille, Jonathan Mougenot, Yann Charles, and Christian Grisolia. Finite element analysis of hydrogen retention in iter plasma facing components using festim. *Nuclear Materials and Energy*, 21:100709, 2019.
- [11] Rémi Delaporte-Mathurin, Etienne Hodille, Jonathan Mougenot, Gregory De Temmerman, Yann Charles, and Christian Grisolia. Parametric study of hydrogenic inventory in the ITER divertor based on machine learning. *Scientific Reports*, 10(1):17798, October 2020. Number: 1 Publisher: Nature Publishing Group.
- [12] Rémi Delaporte-Mathurin, Etienne A. Hodille, Jonathan Mougenot, Yann Charles, Gregory De Temmerman, Floriane Leblond, and Christian Grisolia. Influence of interface conditions on hydrogen transport studies. *Nuclear Fusion*, 61(3):036038, feb 2021.
- [13] George H. Vineyard. Frequency factors and isotope effects in solid state rate processes. *Journal of Physics and Chemistry of Solids*, 3(1):121–127, 1957.
- [14] N. Fernandez, Y. Ferro, and D. Kato. Hydrogen diffusion and vacancies formation in tungsten: Density functional theory calculations and statistical models. *Acta Materialia*, 94:307 – 318, 2015.
- [15] K. Heinola, T. Ahlgren, K. Nordlund, and J. Keinonen. Hydrogen interaction with point defects in tungsten. *Phys. Rev. B*, 82:094102, Sep 2010.
- [16] J. Hou, X. Kong, and X. Wu. Predictive model of hydrogen trapping and bubbling in nanovoids in bcc metals. *nature materials*, 18:833–839, 2019.
- [17] K. Schmid, U. von Toussaint, and T. Schwarz-Selinger. Transport of hydrogen in metals with occupancy dependent trap energies. *Journal of Applied Physics*, 116(13):134901, 2014.
- [18] T. R. Waite. Theoretical treatment of the kinetics of diffusion-limited reactions. *Phys. Rev.*, 107:463–470, Jul 1957.
- [19] L. Gao, W. Jacob, U. von Toussaint, A. Manhard, M. Balden, K. Schmid, and T. Schwarz-Selinger. Deuterium supersaturation in low-energy plasma-loaded tungsten surfaces. *Nuclear Fusion*, 57(1):016026, 2017.
- [20] L. Gao, M. Wilde, A. Manhard, U. von Toussaint, and W. Jacob. Hydrogen atom-ion synergy in surface lattice modification at sub-threshold energy. *Acta Materialia*, 201:55 – 62, 2020.
- [21] James F. Ziegler, Jochen P. Biersack, and U. Littmarck. The Stopping and Range of Ions in Matter. In *Treatise on Heavy-Ion Science*, page 93–129. Pergamon, 1985.
- [22] K. Sugiyama, K. Schmid, and W. Jacob. Sputtering of iron, chromium and tungsten by energetic deuterium ion bombardment. *Nuclear Materials and Energy*, 8:1–7, 2016.
- [23] V.Kh. Alimov, J. Roth, and M. Mayer. Depth distribution of deuterium in single- and polycrystalline tungsten up to depths of several micrometers. *Journal of Nuclear Materials*, 337-339:619–623, 2005. PSI-16.
- [24] E. A. Hodille, Piazza; Z. A., M. Ajmalghan, and Y. Ferro. Hydrogen super-saturated layers in h/d plasma loaded tungsten: A global model based on thermodynamics, kinetics and density functional theory data. *Phys. Rev. Materials*, 2018.
- [25] Yu-Wei You, Xiang-Shan Kong, Xue-Bang Wu, Yi-Chun Xu, Q. F. Fang, J. L. Chen, G.-N. Luo, C. S. Liu, B. C. Pan, and Zhiguang Wang. Dissolving, trapping and detrapping mechanisms of hydrogen in bcc and fcc transition metals. *AIP Advances*, 3(1):012118, 2013.
- [26] C.S. Becquart, C. Domain, U. Sarkar, A. DeBacker, and M. Hou. Microstructural evolution of irradiated tungsten: Ab initio parameterisation of an okmc model. *Journal of Nuclear Materials*, 403(1):75–88, 2010.
- [27] A De Backer, D R Mason, C Domain, D Nguyen-Manh, M-C Marinica, L Ventelon, C S Becquart, and S L Dudarev. Hydrogen accumulation around dislocation loops and edge dislocations: from atomistic to mesoscopic scales in BCC tungsten. *Physica Scripta*, T170:014073, nov.
- [28] Guang-Hong Lu, Hong-Bo Zhou, and Charlotte S. Becquart. A review of modelling and simulation of hydrogen behaviour in tungsten at different scales. *Nuclear Fusion*, 54(8):086001, jul 2014.
- [29] Hong-Bo Zhou, Yue-Lin Liu, Shuo Jin, Ying Zhang, G.-N. Luo, and Guang-Hong Lu. Investigating behaviours of hydrogen in a tungsten grain boundary by first principles: from dissolution and diffusion to a trapping mechanism. *Nuclear Fusion*, 50(2):025016, jan 2010.
- [30] Alexander Bakaev, Dmitry Terentyev, and Evgeny E. Zhurkin. Ab initio study of the stability of h-he clusters at lattice defects in tungsten. *Nuclear Instruments and Methods in Physics Research Section B: Beam Interactions with Materials and Atoms*, 478:269–273, 2020.
- [31] P.M. Piaggi, E.M. Bringa, R.C. Pasianot, N. Gordillo, M. Panizo-Laiz, J. del Río, C. Gómez de Castro, and R. Gonzalez-Arrabal. Hydrogen diffusion and trapping in nanocrystalline tungsten. *Journal of Nuclear Materials*, 458:233–239, 2015.
- [32] Xiao-Chun Li, Xiaolin Shu, Yi-Nan Liu, F. Gao, and Guang-Hong Lu. Modified analytical interatomic potential for a w-h system with defects. *Journal of Nuclear Materials*, 408(1):12–17, 2011.
- [33] K. Heinola, T. Ahlgren, S. Brezinsek, T. Vuoriheimo, and S. Wiesen. Modelling of the effect of elms on fuel retention at the bulk w divertor of jet. *Nuclear Materials and Energy*, 19:397–402, 2019.
- [34] A. Debelle, M.F. Barthe, and T. Sauvage. First temperature stage evolution of irradiation-induced defects in tungsten studied by positron annihilation spectroscopy. *Journal of Nuclear Materials*, 376(2):216–221, 2008.
- [35] M. Zibrov, W. Egger, J. Heikinheimo, M. Mayer, and F. Tuomisto. Vacancy cluster growth and thermal recovery in hydrogen-irradiated tungsten. *Journal of Nuclear Materials*, 531:152017, 2020.
- [36] Pauli Virtanen, Ralf Gommers, Travis E. Oliphant, Matt Haberland, Tyler Reddy, David Cournapeau, Evgeni Burovski, Pearu Peterson, Warren Weckesser, Jonathan Bright, Stéfan J. van der Walt, Matthew Brett, Joshua Wilson, K. Jarrod Millman, Nikolay Mayorov, Andrew R. J. Nelson, Eric Jones, Robert Kern, Eric Larson, C. J. Carey, İlhan Polat, Yu Feng, Eric W. Moore, Jake VanderPlas, Denis Laxalde, Josef Perktold, Robert Cimrman, Ian Henriksen, E. A. Quintero, Charles R. Harris, Anne M. Archibald, António H. Ribeiro, Fabian Pedregosa, and Paul van Mulbregt. SciPy 1.0: fundamental algorithms for scientific computing in Python. *Nature Methods*, 17(3), March 2020.
- [37] Eric Jones, Travis Oliphant, Pearu Peterson, et al. SciPy: Open source scientific tools for Python, 2001–. [Online; accessed 2018-08-10].

- [38] E A Hodille, E Bernard, S Markelj, J Mougenot, C S Becquart, R Bisson, and C Grisolia. Estimation of the tritium retention in ITER tungsten divertor target using macroscopic rate equations simulations. *Physica Scripta*, T170:014033, oct 2017.
- [39] J. Bucalossi, M. Missirlian, P. Moreau, F. Samaille, E. Tsitrone, D. van Houtte, T. Batal, C. Bourdelle, M. Chantant, Y. Corre, X. Courtois, L. Delpech, L. Doceul, D. Douai, H. Dognac, F. Fâisse, C. Fenzi, F. Ferlay, M. Firdaouss, L. Gargiulo, P. Garin, C. Gil, A. Grosman, D. Guilhem, J. Gunn, C. Hernandez, D. Keller, S. Larroque, F. Leroux, M. Lipa, P. Lotte, A. Martinez, O. Meyer, F. Micolon, P. Mollard, E. Nardon, R. Nouaillietas, A. Pilia, M. Richou, S. Salasca, and J.-M. Travère. The west project: Testing iter divertor high heat flux component technology in a steady state tokamak environment. *Fusion Engineering and Design*, 89(7):907–912, 2014. Proceedings of the 11th International Symposium on Fusion Nuclear Technology-11 (ISFNT-11) Barcelona, Spain, 15-20 September, 2013.
- [40] S. Wiesen, D. Reiter, V. Kotov, M. Baelmans, W. Dekeyser, A.S. Kukushkin, S.W. Lisgo, R.A. Pitts, V. Rozhansky, G. Saibene, I. Veselova, and S. Voskoboynikov. The new solps-iter code package. *Journal of Nuclear Materials*, 463:480 – 484, 2015. PLASMA-SURFACE INTERACTIONS 21.
- [41] E. Kaveeva, V. Rozhansky, I. Senichenkov, E. Sytova, I. Veselova, S. Voskoboynikov, X. Bonnin, R. A. Pitts, A. S. Kukushkin, S. Wiesen, and D. Coster. SOLPS-ITER modelling of ITER edge plasma with drifts and currents. *Nuclear Fusion*, 60(4):046019, March 2020. Publisher: IOP Publishing.
- [42] H. Bufferand, G. Ciraolo, Y. Marandet, J. Bucalossi, Ph. Ghendrih, J. Gunn, N. Mellet, P. Tamain, R. Leybros, N. Fedorczak, F. Schwander, and E. Serre. Numerical modelling for divertor design of the west device with a focus on plasma-wall interactions. *Nuclear Fusion*, 55(5):053025, 2015.
- [43] H. Bufferand, P. Tamain, S. Baschetti, J. Bucalossi, G. Ciraolo, N. Fedorczak, Ph. Ghendrih, F. Nespola, F. Schwander, E. Serre, and Y. Marandet. Three-dimensional modelling of edge multi-component plasma taking into account realistic wall geometry. *Nuclear Materials and Energy*, 18:82–86, January 2019.
- [44] J. Denis, J. Bucalossi, G. Ciraolo, E.A. Hodille, B. Pégourié, H. Bufferand, C. Grisolia, T. Loarer, Y. Marandet, and E. Serre. Dynamic modelling of local fuel inventory and desorption in the whole tokamak vacuum vessel for auto-consistent plasma-wall interaction simulations. *Nuclear Materials and Energy*, 19:550–557, 2019.
- [45] K Schmid. Diffusion-trapping modelling of hydrogen recycling in tungsten under ELM-like heat loads. *Physica Scripta*, T167:014025, jan 2016.
- [46] Chaofeng Sang, Zhenhou Wang, Liang Wang, Rui Ding, Qi Wang, Jizhong Sun, and Dezheng Wang. Modeling of fuel retention in the upper tungsten divertor of east from attached to detached divertor plasma. *Fusion Engineering and Design*, 136:908–913, 2018. Special Issue: Proceedings of the 13th International Symposium on Fusion Nuclear Technology (ISFNT-13).
- [47] Hai-Shan Zhou, Hao-Dong Liu, Lu Wang, Xin Yang, Yasuhisa Oya, Ming-Zhong Zhao, Tetsuo Tanabe, Yu-Ping Xu, Xiao-Gang Yuan, Bo Li, Fang Ding, and Guang-Nan Luo. A tritium permeation ‘short cut’ for plasma-facing components of fusion reactors. *Nuclear Fusion*, 59(1):014003, dec 2018.
- [48] A Lasa, J M Canik, S Blondel, T R Younkin, D Curreli, J Drobny, P Roth, M Cianciosa, W Elwasif, D L Green, and B D Wirth. Multi-physics modeling of the long-term evolution of helium plasma exposed surfaces. *Physica Scripta*, T171:014041, jan 2020.
- [49] O.V Ogorodnikova, J Roth, and M Mayer. Deuterium retention in tungsten in dependence of the surface conditions. *Journal of Nuclear Materials*, 313-316:469–477, 2003. Plasma-Surface Interactions in Controlled Fusion Devices 15.
- [50] O. V. Ogorodnikova, J. Roth, and M. Mayer. Ion-driven deuterium retention in tungsten. *Journal of Applied Physics*, 103(3):034902, 2008.
- [51] E.A. Hodille, S. Markelj, T. Schwarz-Selinger, A. Založnik, M. Pečovnik, M. Kelemen, and C. Grisolia. Stabilization of defects by the presence of hydrogen in tungsten: simultaneous w-ion damaging and d-atom exposure. *Nuclear Fusion*, 59(1):016011, nov 2018.
- [52] M. Pečovnik, E.A. Hodille, T. Schwarz-Selinger, C. Grisolia, and S. Markelj. New rate equation model to describe the stabilization of displacement damage by hydrogen atoms during ion irradiation in tungsten. *Nuclear Fusion*, 60(3):036024, feb 2020.
- [53] M. Pečovnik, T. Schwarz-Selinger, and S. Markelj. Experiments and modelling of multiple sequential MeV ion irradiations and deuterium exposures in tungsten. *Journal of Nuclear Materials*, 550:152947, July 2021.
- [54] Lu Sun, Shuo Jin, Hong-Bo Zhou, Ying Zhang, Wenqing Zhang, Y Ueda, H T Lee, and Guang-Hong Lu. Critical concentration for hydrogen bubble formation in metals. *Journal of Physics: Condensed Matter*, 26(39):395402, sep 2014.
- [55] D. Kato, H. Iwakiri, Y. Watanabe, K. Morishita, and T. Muroga. Super-saturated hydrogen effects on radiation damages in tungsten under the high-flux divertor plasma irradiation. *Nuclear Fusion*, 55(8):083019, jul 2015.
- [56] Kazuhito Ohsawa, Fumihiko Nakamori, Yuji Hatano, and Masatake Yamaguchi. Thermodynamics of hydrogen-induced superabundant vacancy in tungsten. *Journal of Nuclear Materials*, 458:187–197, March 2015.
- [57] M. I. Shutikova, N. N. Degtyarenko, and A. A. Pisarev. The Recombination of Tungsten Intrinsic Defects near the Surface Blocked by Hydrogen and Helium Atoms. *Physics of Atomic Nuclei*, 81(11):1580–1585, December 2018.
- [58] C.S. Becquart and C. Domain. An object kinetic monte carlo simulation of the dynamics of helium and point defects in tungsten. *Journal of Nuclear Materials*, 385(2):223–227, 2009. Nuclear Materials III.
- [59] S. Ryabtsev, Yu. Gasparyan, M. Zibrov, A. Shubina, and A. Pisarev. Deuterium thermal desorption from vacancy clusters in tungsten. *Nuclear Instruments and Methods in Physics Research Section B: Beam Interactions with Materials and Atoms*, 382:101 – 104, 2016. The 21st International workshop on Inelastic Ion Surface Collisions (IISC-21).
- [60] T. Ahlgren, P. Jalkanen, K. Mizohata, V. Tuboltsev, J. Räisänen, K. Heinola, and P. Tikkanen. Hydrogen isotope exchange in tungsten during annealing in hydrogen atmosphere. *Nuclear Fusion*, 59(2):026016, jan 2019.
- [61] M. Zibrov, M. Balden, M. Dickmann, A. Dubinko, W. Egger, M. Mayer, D. Terentyev, and M. Wirtz. Deuterium trapping by deformation-induced defects in tungsten. *Nuclear Fusion*, 59(10):106056, sep 2019.
- [62] Sofiane Benannoune, Yann Charles, Jonathan Mougenot, Monique Gaspérini, and Greg De Temmerman. Multi-dimensional finite-element simulations of the diffusion and trapping of hydrogen in plasma-facing components including thermal expansion. *Physica Scripta*, T171:014011, jan 2020.
- [63] A. Durif, M. Richou, G. Kermouche, and J.-M. Bergheau.

Numerical study of the influence of tungsten recrystallization on the divertor component lifetime. *International Journal of Fracture*, January 2021.